

YSO jets in the Galactic Plane from UWISH2: III - Jets and Outflows in Cassiopeia and Auriga

D. Froebrich^{1*}, S.V. Makin¹

¹ Centre for Astrophysics and Planetary Science, University of Kent, Canterbury, CT2 7NH, UK

Received sooner; accepted later

ABSTRACT

We present the analysis of 35.5 square degrees of images in the 1–0 S(1) line of H₂ from the UK Widefield Infrared Survey for H₂ (UWISH2) towards Cassiopeia and Auriga. We have identified 98 Molecular Hydrogen emission-line Objects (MHOs) driven by Young Stellar Objects, 60 % of which are bipolar outflows and all are new discoveries. We estimate that the UWISH2 extended emission object catalogue contains fewer than 2 % false positives and is complete at the 95 % level for jets and outflows brighter than the UWISH2 detection limit. We identified reliable driving source candidates for three quarters of the detected outflows, 40 % of which are associated with groups and clusters of stars. The driving source candidates are 20 % protostars, the remainder are CTTSs. We also identified 15 new star cluster candidates near MHOs in the survey area.

We find that the typical outflow identified in the sample has the following characteristics: the position angles are randomly orientated; bipolar outflows are straight within a few degrees; the two lobes are slightly asymmetrical in length and brightness; the length and brightness of the lobes are not correlated; typical time gaps between major ejections of material are 1–3 kyr, hence FU-Ori or EX-Ori eruptions are most likely not the cause of these, but we suggest MNors as a possible source. Furthermore, we find that outflow lobe length distributions are statistically different from the widely used total length distributions. There are a larger than expected number of bright outflows indicating that the flux distribution does not follow a power law.

Key words: ISM: jets and outflows; stars: formation; stars: winds, outflows; ISM: individual: Galactic Plane

1 INTRODUCTION

The formation of stars via disk accretion of material is inevitably related to mass ejection into jets and outflows along the rotational axis of these objects. The outflows from protostars and Young Stellar Objects (YSOs) were first correctly recognised as such by Snell et al. (1980). Since then numerous studies of these jets and outflows have been conducted to investigate the details of the excitation mechanism, the mass ejection rates, the jet launching, acceleration and collimation, as well as the outflow energetics and timescales (see reviews of e.g. Bachiller (1996), Richer et al. (2000), Bally et al. (2007), Frank et al. (2014)). However, there are still a number of unsolved questions about the outflow phenomenon. Which factors statistically determine the properties (length, luminosity, formation of the main H₂ emission features – knots) of the outflows? Are the properties of the central source (final mass, age) responsible for these or has the environment (density structure in low mass vs. high mass star forming regions) a significant influence? Is the en-

ergy and momentum feedback from the outflows significant enough to explain the local turbulent energy near the forming stars and are the jets and outflows able to terminate the star formation process locally? In order to answer these and similar questions, we need to observationally establish the number of jets and outflows from young stars in the Galactic plane and to determine their average properties.

The first truly large scale work to identify all jets and outflows in a star forming region via an unbiased survey was done in Orion A by Stanke et al. (2002). They utilised the molecular hydrogen rovibrational 1–0 S(1) transition at 2.122 μm . This line is a proven excellent tracer of hot ($T \sim 2000$ K) and dense ($n \geq 10^3 \text{ cm}^{-3}$) gas excited by the fast shocks ($10 - 100 \text{ km s}^{-1}$) caused by the interactions of jets and outflows with the surrounding interstellar medium. As the line is in the K-band, it is less influenced by extinction compared to other tracers of these shocks such as optical H α or [SII] lines, which are the historically used tracers for Herbig-Haro objects. It is usually also stronger than the near infrared (NIR) [FeII] lines, except in strong shocks or purely atomic environments. Observations in other molecular outflow tracers, such as CO or SiO,

* E-mail: df@star.kent.ac.uk

on large (molecular cloud) scales typically lack the combination of spatial resolution and depth to identify the fainter outflows, which are detectable in the NIR, especially in complex regions along the Galactic plane. Furthermore, the $1-0S(1)$ line flux is proportional to the total outflow luminosity for a range of excitation conditions (Caratti o Garatti et al. 2006). Note that despite the shock velocity and gas density limitations for the excitation of the $1-0S(1)$ transition, at least some parts of the vast majority of jets and outflows from YSOs are detectable in this line.

After the pioneering work by Stanke et al. (2002), further searches for jets and outflows in star forming regions have been conducted e.g. by Walawender et al. (2005), Hatchell et al. (2007), Davis et al. (2009) and Khanzadyan et al. (2012). In order to establish a truly unbiased sample of jets and outflows from young stars in the Galaxy, not restricted to nearby, mostly low-mass star forming regions, the UKIRT Widefield Infrared Survey for H_2 (UWISH2) was conducted by Froebrich et al. (2011). In this series of papers we are analysing in detail the identified jets and outflows from young stars in this survey as Molecular Hydrogen emission-line Objects (MHOs) defined in Davis et al. (2010). Previous works based on UWISH2 data by Ioannidis & Froebrich (2012a,b) have concentrated on the Serpens and Aquila region along the plane, while Lee et al. (2012, 2013) have investigated H_2 outflows from Spitzer-detected extended green objects.

This paper is structured as follows: In Sect. 2 we briefly discuss the data and our analysis procedures such as the identification of the MHOs and their most likely driving sources. The results, outflow and driving source properties, are then discussed in detail in Sect. 3.

2 DATA ANALYSIS

2.1 UWISH2 data

Our analysis uses data from the UKIRT Widefield Infrared Survey for H_2 by Froebrich et al. (2011) and its extension towards the Cygnus X and Cassiopeia/Auriga regions discussed in Froebrich et al. (2015). All images are taken with the Wide Field Camera (Casali et al. 2007) at the UK Infra-Red Telescope. A total exposure time of 720 s per pixel was obtained through the $1-0S(1)$ filter at $2.122 \mu\text{m}$. Utilising micro-stepping during the observations, the final images have a pixel size of $0.2'' \times 0.2''$ and the typical seeing in the data is $0.8''$. Averaged over this typical seeing, the typical 5σ surface brightness detection limit in the data is $4.1 \times 10^{-19} \text{ W m}^{-2} \text{ arcsec}^{-2}$.

In this paper we only analyse the data taken towards the region of Cassiopeia and Auriga. This covers Galactic Longitudes from approximately $l = 140^\circ$ to $l = 155^\circ$ and Galactic Latitudes from $b = -4^\circ$ to $b = 3^\circ$. The detailed coverage of the field is shown in Fig. 1. The observed fields cover a total of 35.46 square degrees. For the entire area we also have broad-band JHK data from the UKIDSS (Lawrence et al. 2007) Galactic Plane Survey (Lucas et al. 2008). The K-band images have been utilised to continuum subtract the H_2 images following the procedures described in Lee et al. (2014).

2.2 MHO and driving source identification

The identification of jets and outflows from young stars, or MHOs – as defined in Davis et al. (2010), and their respective driving sources has been done in the following way:

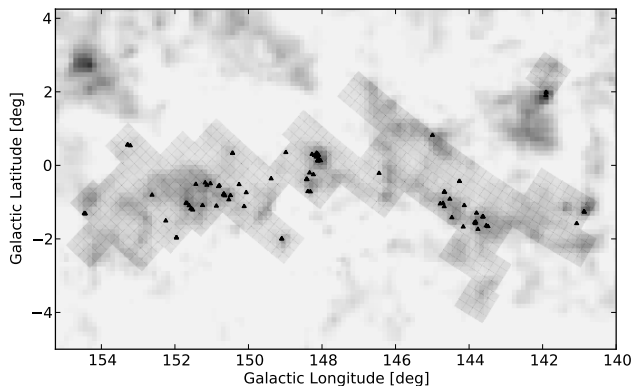


Figure 1. Coverage of the survey along the Galactic plane in Cassiopeia and Auriga with UWISH2 tiles in Galactic Coordinates. Observed fields are indicated by the slightly darker grid regions. Overplotted as black triangles are the positions of all detected MHOs in this area. The background image are the CO data from Dame et al. (2001); darker colours indicate higher levels of CO emission.

- We selected all H_2 emission line features that were catalogued by Froebrich et al. (2015) in the Cassiopeia and Auriga region of UWISH2. There were 51 groups of jets features with a total of 187 individual H_2 emission line objects in this area. These groups were originally defined in Froebrich et al. (2015) only based on their spatial distribution. Here we set out to identify the individual outflows in each of these groups.

- Each of the groups was investigated in detail by inspecting the H_2 -K difference images and JKH_2 colour composite images. We tried to assign the individual H_2 features in each group to as few as possible jets/outflows. The decision of which H_2 emission line object belongs to which potential outflow has been based on the appearance/shape of the emission feature, and the alignment of features with each other and/or the potential driving source. Each identified outflow has subsequently been assigned a unique MHO number. H_2 features (or small groups thereof) without an obvious driving source candidate have also been given a unique MHO number if their appearance suggests they represent emission from shocked gas. H_2 features that are most likely caused by radiative excitation/fluorescence have been disregarded from any further analysis.

- We also searched the H_2 -K and JKH_2 images near the pre-selected groups of jet features for objects that have been missed in the original catalogue. These objects were missing as they did not meet the selection criteria in Froebrich et al. (2015). Most of the identified outflows have one or a few H_2 emission knots that have a surface brightness that prevented their inclusion in the original list.

- As MHO coordinates we use the coordinates of the candidate driving source if one can be identified. For MHOs consisting of single or multiple knots without source candidate, the mean coordinates of the knots are used as MHO position.

- Driving source candidates were identified based mainly on their alignment with the potential outflow direction. Furthermore, we considered the NIR or mid-IR colours/detections of potential source candidates as well as the K-band variability and the presence of nebulosities near potential sources. Based on these criteria and the resulting number of potential driving sources nearby, we assigned a likelihood to each identified source that indicates how certain we are that the correct source has been identified for the H_2 features. In some cases the position of the suspected driving source is clear, but there is no detection in any catalogue or the literature. In these cases we have manually determined the suspected source

position and indicated this scenario with *noname* as the source identification for the MHO.

2.3 Determination of MHO and driving source properties

After the identification of the individual MHOs as outflows or groups of individual H₂ features, we grouped the MHOs into a number of categories and determined the properties for each MHO as well as those of the driving sources. The details of this process are as follows:

- MHOs are categorised as either bipolar outflows, single-sided outflows or just an individual/small group of H₂ emission knots.
- For all MHOs, sub-features are identified and labelled by letters. We start at one end of the outflow with 'A' and knots are labelled with sequential letters along the outflow axis. For groups of H₂ features without a source, there is no systematic pre-described order in which the labelling of the sub-features is done.
- For each identified outflow lobe, the length of the lobe from the potential source to the most distant end of the H₂ knot is measured, as well as the position angle of the lobe with respect to the North direction. For all bipolar outflows, the difference of the two position angles from a perfect parallel orientation of the two lobes is calculated.
- For each outflow lobe with more than one H₂ emission knot, all the gaps/distances between succeeding knots are measured.
- Photometry is done separately for each H₂ knot that has been assigned to any of the MHOs. All knots are outlined with polygons enclosing the area considered to be part of the H₂ emission feature and the total integrated flux inside the polygon is measured. Care has been taken to exclude any continuum point sources superimposed on the H₂ emission from the flux measurements, and also low surface brightness areas are included, which were not picked up in the automatic H₂ feature detection used in Froebrich et al. (2015). For each MHO a nearby, H₂ emission-free area of the image has been selected to estimate the 'local' background flux. The calibration of the fluxes has been done in the same way as described in Froebrich et al. (2015).
- For each identified MHO driving source we estimate the likelihood that we have selected the correct source, based on the number of nearby potential source candidates and their properties. We also categorise each MHO according to whether it is likely to come from a driving source situated in a cluster or group of stars, or if the potential source is isolated.
- For each driving source the coordinates and designations (e.g. 2MASS, WISE, or IRAS IDs) are collected. If a source is detected in multiple catalogues, we use the coordinates of the object in the catalogue with the shortest wavelengths, as these usually have the highest spatial resolution.
- For each driving source the near- and mid-IR magnitudes from 2MASS, GPS and WISE are collected. We determine the K-band variability for all objects that have more than one K-band magnitude available.
- We utilise the WISE magnitudes to determine the spectral index α of the SED following Majaess (2013), where positive values denote colder objects and negative values warmer objects. We use the α value to sort the driving source candidates with WISE detections into an age sequence. Hereafter we split the sample into younger and older objects at $\alpha = -0.5$, which ensures a 50/50 split of the objects into the two groups. Note that the younger sample will hence contain protostars and CCTTs, i.e. the two samples do not represent a split into the two evolutionary stages.

3 RESULTS AND DISCUSSION

3.1 The Cassiopeia and Auriga MHO catalogue

From the investigated 51 groups of H₂ features, 46 (90 %) are found to contain emission knots which most likely are caused by shock excitation from jets and outflows from young stars. Two of the five groups without MHOs are most likely caused by fluorescently excited molecular cloud edges. Two further objects are most likely variable stars (note that the H₂ and K-band images are taken up to several years apart), and one object seems to be an image artefact from a bright star. In total there are 15 (8 %) individual H₂ features, originally classified as 'jet' in Froebrich et al. (2015) that after detailed investigation have been judged not to be shock excited emission. The majority (12 or 6.4 %) are most likely associated with fluorescently excited molecular cloud edges. Only 3 (1.6 %) of the H₂ features are artefacts or variable stars. Thus, even given the small sample size, one can conclude that the full UWISH2 catalogue from Froebrich et al. (2015) contains fewer than 2 % false positive detections of H₂ features, and the fraction of misclassified 'jet' features in the catalogue is well below 10 %.

In the 46 groups with jet/outflow-like features we have identified 98 individual MHOs. Thus, the average number of outflows per jet group is about two. Hence, scaled up to the full UWISH2 catalogue there will be about 1500 outflows from young stars. We have overplotted the positions of all MHOs on the CO data from Dame et al. (2001) in Fig. 1. As expected, the objects are mostly concentrated towards the high column density CO features. They are also clustered in groups of a few, similar to what has been found in previous studies along the Galactic plane in Serpens and Aquila by Ioannidis & Froebrich (2012a).

There are 57 (58 %) bipolar and 17 (17 %) single-sided outflows amongst the 98 MHOs. For the remaining 24 (24 %) MHOs, which are groups of or individual H₂ knots, no convincing source candidate could be identified. Driving source candidates have been identified for all the bipolar and single-sided objects. Note that all MHOs in this regions are new discoveries. Potentially the only known outflow might be MHO 2982 with the source candidate AFGL 490-iki (IRAS 03234+5843) which has been discovered as a roughly North-South orientated CO-outflow in Lyder et al. (1998). The H₂ detection in our data coincides with the redshifted lobe of the CO data.

Many of the MHOs have H₂ emission knots which are not included in the full UWISH2 catalogue. However, only four of the MHOs (4 %) had none of their H₂ knots in the catalogue. Thus, the list of Froebrich et al. (2015) has a completeness of the order of 95 % or higher for H₂ emitting jets and outflows from young stars brighter than the UWISH detection limit.

In Table A1 we list all the properties of the identified MHOs. This includes the following: i) the MHO number; ii) Right Ascension of the object; iii) Declination of the object; iv) Length of the outflow lobe(s); v) Position angle of the outflow lobe(s) from North over East; vi) Flux of the outflow lobe(s) or knots; vii) Type of outflow (B - bipolar, S - single-sided, K - single or group of knots without apparent source candidate); viii) Is the MHO associated with cluster or group of stars? ix) Source candidate identification; x) Likelihood P_S that source candidate is the real driving source; xi)–xiii) Near-infrared JHK magnitudes of the source candidate; xiv)–xvii) Mid-infrared WISE magnitudes of the source candidate; xviii)–xxii) Is there a detection of the source candidate in the following surveys/catalogues: G – UKIDSS GPS, 2 – 2MASS, W – WISE, A – AKARI, I – IRAS? In the Appendix table we also

show the H_2 -K difference and JKH_2 colour composite images for all MHOs together with some additional notes on each object.

3.2 The driving source properties

We have identified a driving source candidate for 74 (76 %) of the MHOs, i.e. for all the single-sided and bipolar outflows. Note that some MHOs have the same source candidate (e.g. MHO 1070, 1071, 1072). Even if we could not find a convincing source candidate for the remaining MHO objects, it is possible to judge whether the driving source is likely to be in a group or cluster of stars, or isolated. In total 40 (41 %) of the potential driving sources are associated with clusters or groups of stars, while 58 (59 %) seem to be isolated. As the majority of the young protostars ($\alpha > 0$) and CTTs ($\alpha < 0$) are situated in clusters a larger fraction of potential driving sources are expected to be associated with clusters. A similar result has been found for outflows in Orion A by Davis et al. (2009). This seems to indicate that either clustered star formation inhibits the formation of outflows or that due to the shortness and early onset (a larger fraction of protostars drive outflows compared to CTTs) of the outflow active state, the sources in clusters identifiable in the NIR data are simply older than the isolated sources. Thus, the observed percentages could simply reflect an evolutionary trend. This is somewhat supported by the fact that 28 % of sources in clusters are in the younger group, while this is the case for 41 % of the isolated sources.

In total we have identified 15 as-yet unknown cluster candidates and seven apparent groups of YSOs near the MHOs in the survey area. Several of these new clusters are compact and associated with IRAS sources. We list their positions, apparent radii and the estimated number of cluster members visible in the NIR images in Table 1. Our distinction of 'clusters' and 'groups' has been based on the number of potential members as well as the distribution of them. Where the distribution appears circular the object is classified as cluster even if the number of visible members is low. If the number of members is low and they seem to be following a more 'filamentary' distribution the object is classified as a group. Note that we have not performed an exhaustive, complete search for clusters in the entire survey area discussed here. Thus, the number of so far undiscovered clusters in the survey area is potentially much higher.

Of all driving source candidates 59 (80 %) have a WISE detection in all four filters. The classification of the objects based on the WISE fluxes following (Majaess 2013) shows that 10 (17 %) have positive slopes (α), while 49 (83 %) have a negative slope of the SED, indicating a mix of CTTs and protostars as the driving sources for the detected outflows. We also investigated the NIR colours of the sources. For 23 (31 %) objects we found a 2MASS counterpart, and 35 (47 %) are detected in GPS. Figure 2 shows the NIR colour-colour diagram of all the source candidates. Most objects are below or at the bottom of the reddening band, indicating CTTs and protostars as driving sources.

In total 23 (31 %) of the source candidates have more than one K-band detection (i.e. GPS and 2MASS) and we investigate their K-band variability between the two surveys. Of these objects, 16 (70 %) show a variability of more than 0.1 mag, and 4 (17 %) vary by more than 0.5 mag over a typical timescale of several years. Only 4 objects have two epochs of observations in GPS, none of them varies by more than 0.1 mag between these two epochs.

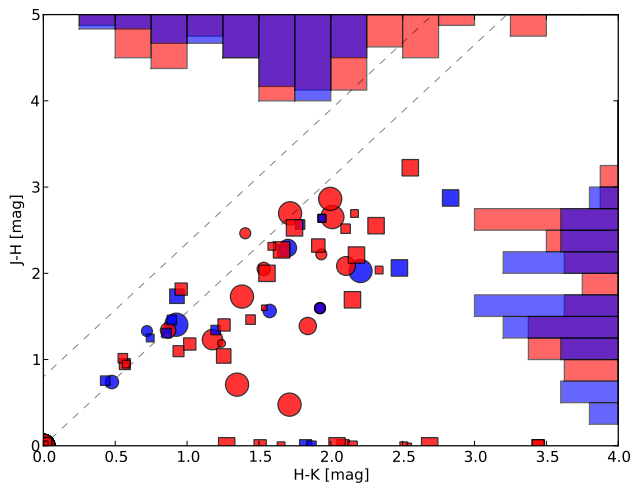


Figure 2. NIR colour-colour-diagram of the identified candidate outflow driving sources. The dashed lines indicate the standard reddening band for stellar atmospheres. Square symbols indicate GPS detections, while circular symbols indicate 2MASS data. Red (lighter) symbols are for bipolar outflows, while the blue (darker) symbols are for single-sided MHOs. The size of the symbols indicates the probability assigned to each source candidate that the identification is correct. The histograms show the NIR colour distribution of the source candidates (red/light for GPS and blue/dark for 2MASS).

3.3 The MHO properties

40 MHOs have potential source candidates inside or associated with (nearby, potentially triggered SF) young clusters, while 58 MHOs have potential sources with no apparent connection to a clustered environment. Of the bipolar objects, 24 (42 %) are associated with clusters and 33 (58 %) are not. Hence the visibility of one or two of the outflow lobes does not depend on the environment. Note that "clustered environment" in this region typically refers to clusters or groups with 10–50 NIR visible stars and not massive clusters (with a few exceptions).

3.3.1 Jet/Outflow orientation

We have measured the position angle of all single-sided and bipolar outflows as the angle between the vector pointing from the source candidate along the outflow lobe and the North direction (towards East). For bipolar outflows the position angles of the two lobes are measured separately and are averaged. In a final step the position angles are taken modulus 180° . In Fig. 3 we show the distributions of the position angles separated for single-sided and bipolar outflows.

The distribution shows no apparent inhomogeneities. We used a 2-sample Kolmogorov-Smirnov (KS) test to investigate if the position angles are in agreement with a homogeneous distribution of angles between 0° and 180° . For the bipolar outflows we find a probability $p > 0.9999$ that the position angle distribution and a homogeneous distribution are drawn from the same parent sample. For the single-sided outflows we find $p = 0.986$ and for all outflows combined $p = 0.997$. Furthermore, $p = 0.988$ that the position angle distribution for bipolar and single-sided outflows is drawn from the same parental distribution. We also determined the vector representing the mean position angles (taken as unit vectors) and of all lobes of the bipolar outflows. This mean angle vector

Table 1. Summary table listing the properties of the newly discovered clusters and groups of stars near the MHOs. We list: i) The cluster ID; ii) The cluster Right Ascension (J2000) in degrees; iii) The cluster Declination (J2000) in degrees; iv) The apparent cluster radius in arcminutes; v) C – object most likely a cluster; G – object most likely just a small group of stars; vi) Estimated number of near-infrared visible members; vii) ID numbers of MHOs with driving sources in the cluster; viii) Notes on each object such as the association with known objects.

ID	RA [deg]	DEC [deg]	R ["]	C/G	Stars	MHO	Notes
01	51.111	55.204	0.35	C	50	2986,2987,2988	coincides with IRAS 03205+5501
02	61.124	51.404	0.65	C	40		no known associations
03	60.831	51.487	0.77	C	30	1068	no known associations
04	61.880	50.513	0.40	C	30		coincides with IRAS 04037+5022
05	50.993	55.186	0.46	C	30		no known associations
06	61.638	50.508	0.55	C	20	1087	no known associations
07	62.061	50.519	1.24	C	20	1090,1091	coincides with IRAS 04045+5023, very extended
08	52.990	55.646	0.27	C	20	2996,2997	coincides with IRAS 03281+5528
09	61.362	49.652	0.37	C	15	1092,1093,1094	1' north of HII region, classified as Galaxy (LEDA 2348913)
10	63.340	50.056	0.23	C	15	1096	no known associations
11	61.486	51.451	0.19	C	10	1078	dominated by bright nebulous star 2MASX J04055657+5127052 (Galaxy)
12	65.569	50.572	0.25	C	10	1097,1098	no known associations
13	65.468	50.610	0.47	C	10	1099	coincides with IRAS 04181+5029
14	53.289	55.174	0.41	C	10	3700,3701,3702	0.5' South of HII region MSX6C G144.6678-00.7136
15	56.295	54.528	0.25	C	10	3707	0.5' East of IRAS 03412+5422
16	61.090	51.396	0.40	G	15	1073,1074	near HII region, classified as Galaxy (2MASX J04041342+5122587)
17	61.955	51.257	1.13	G	15	1081	coincides with IRAS 04040+5107
18	62.015	50.492	0.39	G	15		no known associations
19	61.013	51.378	0.32	G	10	1070,1071,1072	about 8' from large HII region NGC 1491
20	61.731	50.500	0.20	G	10	1085	no known associations
21	50.659	55.061	0.18	G	10	2984,2985	coincides with IRAS 03188+5452
22	51.617	54.682	0.08	G	5	2995	coincides with IRAS 03226+5430

has a length of 0.009 units, hence showing as well that the position angles are homogeneously distributed.

We also investigate the differences in position angles for the two sides of the bipolar outflows. Typically the outflows are straight, with a median difference in the position angles between the two lobes of 5.0° . There are only a few objects (8/57) for which the two sides have a position angle difference of more than 10° .

In total 12 (12%) of the MHOs are part of X-shaped regions (e.g. MHO 1092, 1093, 1094) where there seem to be two or more outflows originating from the same source at about 90° from each other. Lee et al. (2016) have shown that binary outflows seem to be orientated randomly or even preferentially perpendicular with respect to each other. Hence, all these groups could be originating from binaries. Another typical sign for a binary source is precession of the outflow. In total there are only 4 MHOs with clear signs of precession. Half of them are part of the X-shaped regions.

3.3.2 Jet/Outflow length

We have measured the lengths of both outflow lobes in all the bipolar objects identified. In Fig. 4 we show the length ratio (R_L), which we define as the ratio of the length of the shorter lobe and the length of the longer lobe. Hence, completely symmetrical objects have a length ratio of one, and all values are between zero and one. As one can see, there is an almost homogeneous distribution of R_L values between 0.6 and 1.0. The median length ratio of all bipolar objects is $R_L = 0.72$. Hence, the typical bipolar outflow is somewhat asymmetric. However, highly asymmetric objects are rare. For example there are only 12/57 = 21% of objects with $R_L < 0.5$, and a large fraction of these have low probability source candidates.

We find that $p = 0.135$ when we test if the R_L distributions for bipolar objects in and not in clusters are drawn from the same parent distribution. There seems to be a slightly higher fraction of asymmetric objects associated with clusters. If the structure of the

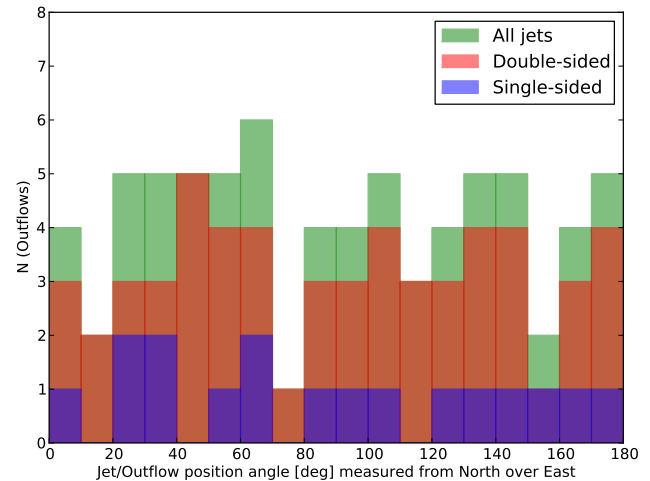


Figure 3. Outflow position angle distribution for all MHOs with a driving source candidate. The different coloured histograms indicate the single-sided and bipolar, as well as all outflows.

environment is responsible for the formation of bright H_2 knots, then a more clumpy interstellar medium (expected near clusters) would lead to more asymmetric length ratios. However, as evident from Fig. 4 most of the driving source candidates of the asymmetric outflows have a low source probability. Hence there is currently no statistically significant difference in the asymmetry distribution of outflows from clustered sources and isolated objects.

3.3.3 Jet/Outflow length distribution

In the left panel of Fig. 5 we show the distribution of projected lobe lengths for the outflows, separated into bipolar and single-sided ob-

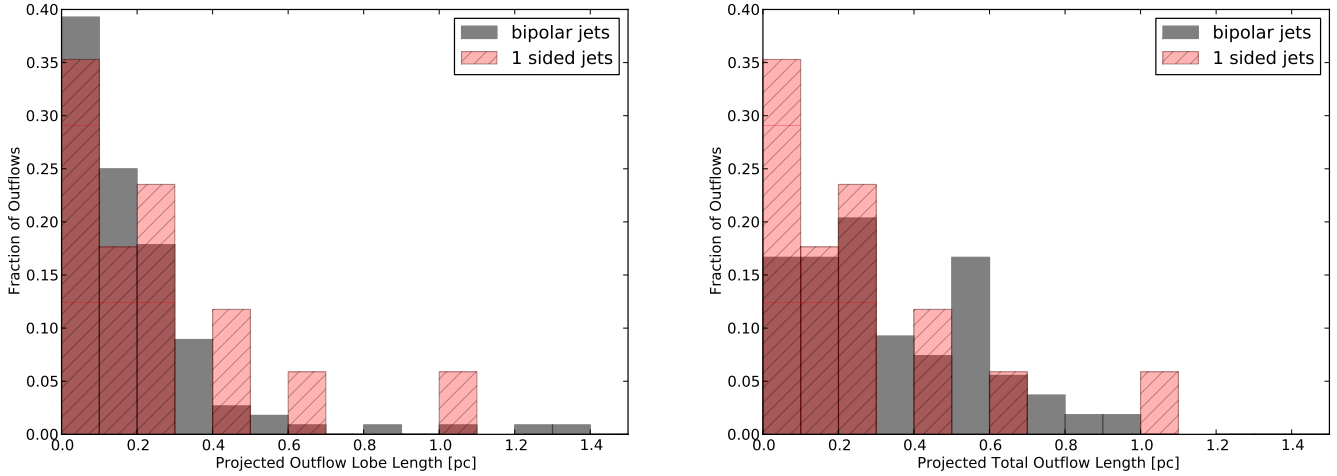


Figure 5. Distribution of outflow lobe (left) and total, end-to-end (right) lengths for bipolar and single-sided objects. All histograms are normalised to the same total number of objects.

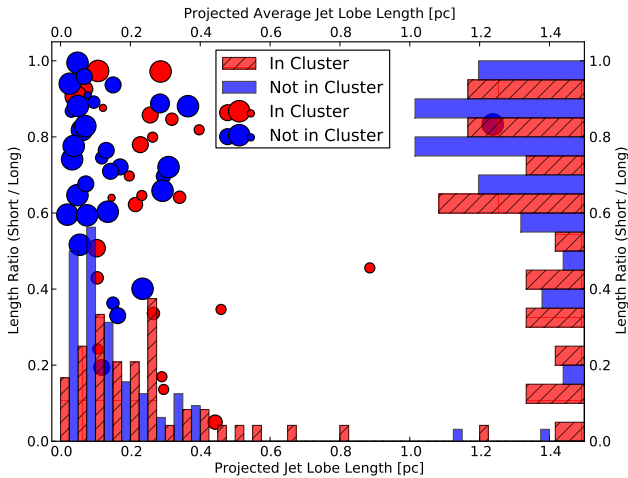


Figure 4. The circles indicate the length ratio (short over long) of the two lobes of the detected bipolar outflows plotted against the average lobe length of the MHOs. The circle size is proportional to the source probability. The histograms show the distributions of the projected lobe lengths and length ratio. The histograms for sources in clusters and not in clusters are normalised to the same number of objects.

jects. As expected there are more shorter outflows than longer ones. It seems that the fraction of longer outflow lobes is increased for the single-sided objects. But small number statistics is an issue and a KS-test is also indecisive. We find $p = 0.53$ that both distributions are drawn from the same parent sample. Note that some of this could be explained by potential systematic misidentification of driving sources for the single-sided objects.

As most of the literature uses the total lengths of jets and outflows (end-to-end for bipolars and source-to-end of single-sided objects) to investigate the length distributions we compare them in the right panel of Fig. 5. As one can see, the total length distribution for the bipolars differs significantly from the lobe length distribution. There are far fewer short objects when measuring the total length. The KS-test shows that the total length distribution of the single-sided and the bipolar outflows are most likely drawn from different distributions ($p = 0.18$). Hence, mixing the two types of objects

into a common length distribution should be avoided. Furthermore, due to the typical asymmetry of the bipolar jets (see Sect. 3.3.2), the lobe length and total length distributions of the bipolars are very different ($p = 4.644 \times 10^{-4}$).

We compare the lobe length distribution of the bipolar outflows with sources associated with clusters and those not. The two distributions are shown as histograms in Fig. 4. The fraction of objects with a short lobe length is much higher for objects not associated with clusters. The KS-test results in $p = 0.0014$ that the distributions are from the same parent sample. Hence, the more isolated bipolar outflows seem to be shorter. Indeed the median lobe length for clustered objects is 0.22 pc, while for the non-clustered objects the median is only 0.09 pc, less than half. This, to some extent, can be explained by the larger fraction of highly asymmetric outflows found to be associated with clusters (see Sect. 3.3.2). Hence, objects associated with clusters will have one of their lobes much longer than the average. There is a possibility that some of this is a distance bias, i.e. apparently isolated objects are more distant, and hence the clusters are not visible. We cannot rule this out entirely, as there are no individual distances for all objects and the distance measurement method applied by Ioannidis & Froebrich (2012b) will not work in this area due to the lack of sufficient foreground stars.

We also tested if the lobe length distributions for outflows from younger and older driving sources are different. The KS test is indecisive leading to $p = 0.55 - 0.65$, depending on whether all lobe lengths or only the bipolar outflows are considered. The only slight difference between the two groups of lobe lengths is that most of the longest (> 0.5 pc) lobes are associated with older driving sources.

3.3.4 Gaps between H_2 knots

In Fig. 6 we show the distribution of gaps between the main (isolated) H_2 emission knots in the jets and outflows. These larger knots represent either major mass ejection/accretion events or the position of denser regions in the environment. The median gap is about 0.19 pc, and the mean is 0.25 pc, which converts to about 2–3 kyr between the knots at the assumed distance of 2 kpc and a projected transversal speed of 80 km/s (assumed to be constant). There is a range of the most common knot gaps between 0.05 pc and 0.25 pc,

corresponding to 1–3 kyr between ejections. These numbers are similar to what has been found for outflows in Serpens and Aquila by Ioannidis & Froebrich (2012b), who showed that the typical gaps between large H₂ knots correspond to 1–2 kyr.

As seen in Sect. 3.3.3, the dynamical timescales of the outflow lobes, estimated from their typical total lengths, amount to values that range from the above determined few kyr to about 10 kyr for the parsec scale outflows. Hence, if the main knots in outflows are generated by major mass ejection events, then they should occur typically every few kyr for the jet-driving young stellar objects. Given the estimates for the FU-Ori occurrence rates of 5–50 kyr (Scholz et al. 2013), it is highly unlikely that FU-Ori type events are the cause of the main H₂ knots. Similarly, EX-Ori are also not suitable candidates for causing these knots, as these bursts repeat semi-regularly every one to ten years. Recent NIR monitoring of large parts of the Galactic Plane (in UKIDSS GPS, Contreras Peña et al. (2014); VISTA VVV, Contreras Peña et al. (2016)) reveals a large number of variables with characteristics in-between the FU-Ori and EX-Ori classifications. Dubbed MNors by Contreras Peña et al. (2016), these apparently more common eruptions might be the cause of the main H₂ knots in outflows. Further statistics are required however, to establish if the occurrence rate of the MNor eruptions correspond to the typical time gaps between the outflow knots.

We separated the gaps in the outflows based on the slope of the spectral energy distribution of the driving source. We use $\alpha = -0.5$ as the separator of young and old objects. The two distributions for the gaps between knots are also shown in Fig. 6, where each main bin is separated into the two bins for younger and older sources. While the basic distributions seem to look the same, they are in fact different ($p = 0.14$). Both the mean and median gap sizes decrease by 70 % from the younger to the older driving sources. Of the ten largest gaps between knots, only one of them is associated with an older driving source.

Despite the low p -value it is not clear if this difference is caused by small number statistics or indeed real. In a future paper we will study the outflows in the Cygnus X region, where we have identified between four and five times as many objects as in Cassiopeia and Auriga. One would expect that younger sources have a higher frequency of accretion bursts and hence mass ejection events (e.g. Vorobyov & Basu (2006)). Thus, the gaps between knots should be, on average, smaller in outflows from younger driving sources if the typical ejection speeds are comparable. Even if the density structure near the driving sources governs the H₂ knot formation, one would expect a more clumpy medium near younger sources and hence smaller gaps between knots.

One can combine the results from Sect. 3.3.3 (longer outflows originate more commonly from older sources) and this section (there are smaller gaps between knots in outflows from older objects). This leads to the conclusion that on average, there are more knots per outflow lobe length in the outflows from older sources. Thus, even considering potentially variable speeds for the ejection of material, the frequency of the formation of larger H₂ knots is higher for older driving sources. Note that this is based on small number statistics and will be revisited in our future paper discussing the outflows identified in Cygnus X. Furthermore, there is a possibility that some of the knots from younger sources are not detected due to higher extinction levels.

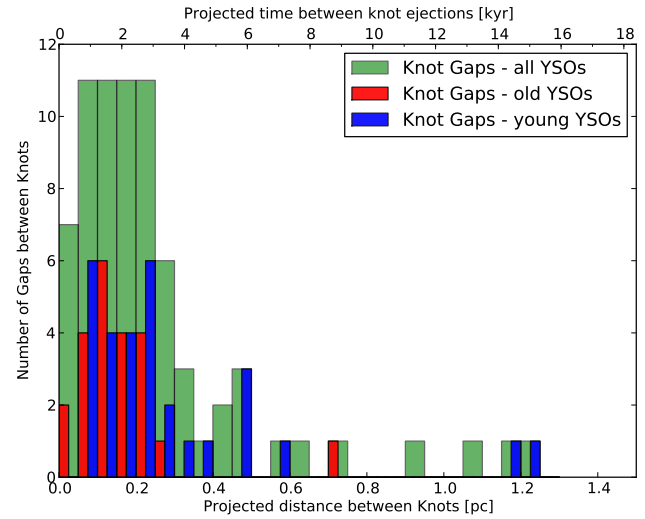


Figure 6. Distribution of gaps between individual outflow knots. Younger and older YSOs are separated using $\alpha = -0.5$.

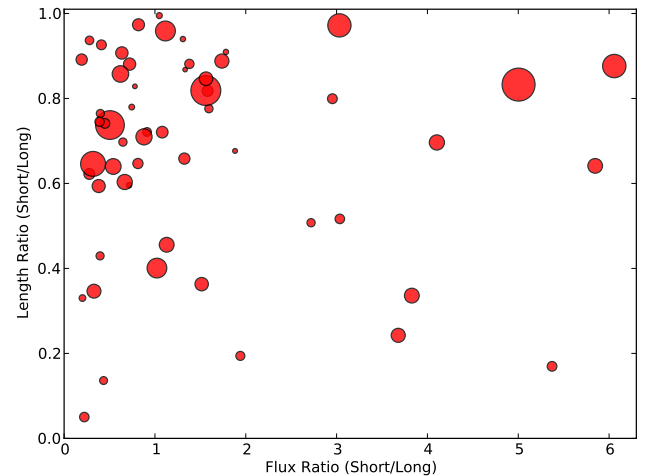


Figure 7. Jet length ratio plotted against the flux ratio of the lobes for all bipolar jets. The size of the circles indicates the total flux of the outflow.

3.3.5 Jet/Outflow flux distribution

Figure 7 shows that there is no correlation between flux ratio and length ratio of the two lobes in bipolar outflows. Both ratios are estimated as the values (length or flux) of the short side divided by the value of the long side, hence all length ratios are less than one. About half of the bipolar objects have a flux ratio less than one and half a flux ratio larger than one. This percentage also does not depend on the flux itself. Essentially, the brightness ratio of the two lobes in bipolar jets/outflows is statistically independent of the length ratio of the same two lobes.

In Fig. 8 we show the flux distributions of all H₂ knots (right panel) as well as the flux distributions of all outflow lobes (left panel). Generally the flux distributions are better fit by exponentials than power laws, due to a number of bright ‘outliers’. They are too frequent for the entire distribution to be power laws and are caused by some of the very long outflows in our sample. Generally the rms of the power law fits are about twice as high as for the exponential fits of the distributions. Essentially distributions start

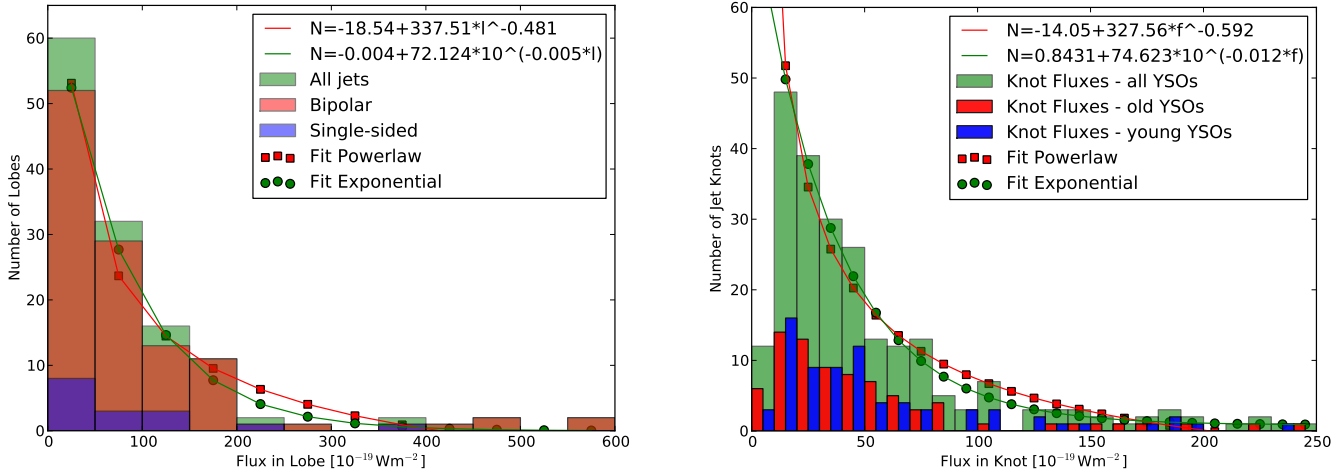


Figure 8. Flux distribution of the outflow lobes (left) and the individual knots (right). Some objects have fluxes higher than the largest values along the x-axis in the graphs and are not shown.

to deviate from power laws at fluxes above $15 \times 10^{-18} \text{ W m}^{-2}$ for the individual H_2 knots and $30 \times 10^{-18} \text{ W m}^{-2}$ for the fluxes in the outflow lobes. When fit by power laws, the lobe flux distribution follows $N \propto F^{-0.5}$ while the flux distribution of the individual knots in the outflows is a bit steeper with $N \propto F^{-0.6}$. These numbers do not change if only those objects below the above quoted flux limits are used for the fits. However, in these cases the exponential fits are still resulting in a lower *rms*. Generally the power law exponents are in agreement with the values for the luminosity distributions of outflows in Serpens and Aquila by Ioannidis & Froeblich (2012b) who found $N \propto F^{-0.5 \dots -0.7}$. Note that these are measured as a mix of bipolar and single-sided outflows.

The measured fluxes of the outflows can be converted into luminosities with our assumed distance for all objects of 2 kpc. In this case, a flux of $5 \times 10^{-18} \text{ W m}^{-2}$ (corresponding to the median lobe flux in our sample) converts to about $0.6 \times 10^{-3} L_{\odot}$ in the 1–0 S(1) line of H_2 . This median luminosity is at the faint end of the luminosity distribution of outflows investigated along the Galactic plane in Serpens and Aquila by Ioannidis & Froeblich (2012b). This is caused by the fact that the typical distances for the objects in this study were 3–5 kpc (compared to our 2 kpc) while the median flux of the two samples is almost identical. Thus, the MHO sample investigated here includes a number of intrinsically fainter objects that fell below the detection limit in the study by Ioannidis & Froeblich (2012b). However, the number of MHOs with a brightness above $10^{-3} L_{\odot}$, normalised to the distance-corrected projected survey area is comparable in both studies. In Cassiopeia and Auriga this number is only about 30 % lower than in Serpens and Aquila.

We investigated if the evolutionary stage (α) of the driving sources influences the flux distributions. However, as can be seen in the right panel of Fig. 8 there are no differences in the flux distribution of H_2 knots of outflows from younger and older driving sources ($p = 0.94$). Similarly the flux distribution for the outflow lobes of younger and older driving sources are similar with $p = 0.93$.

The right-hand side histogram in Fig. 8 also indicates that our completeness limit for the detection of outflow knots is of the order of $10^{-18} \text{ W m}^{-2}$. This compares well with the estimated 5σ surface brightness detection limit in UWISH2 of $4.1 \times 10^{-19} \text{ W m}^{-2} \text{ arcsec}^{-2}$ (Froeblich et al. 2015), since most of the knots are extended over more than a few square arcseconds.

4 CONCLUSIONS

We have analysed the population of jets and outflows from young stars in a 35.5 square degree region along the Galactic Plane in Cassiopeia and Auriga utilising H_2 imaging data from the UWISH2 survey (Froeblich et al. 2011) and the catalogue of potential jet/outflow features from Froeblich et al. (2015). In the investigated area we have identified 98 Molecular Hydrogen emission-line Objects, i.e. potential jets and outflows from young stars, all of which are new discoveries. When scaled up to the entire UWISH2 survey, we thus expect a total sample of about 1500 MHOs for analysis.

The detected MHOs are classified as bipolar outflows (60 %), single-sided outflows (20 %) and individual or small groups of H_2 knots (20 %). Comparing the number of identified MHOs to the automatically generated and classified catalogue of UWISH2-detected H_2 features, we can conclude that the catalogue from Froeblich et al. (2015) contains much less than 10 % of false positives amongst the H_2 features classified as jets and outflows from young stars. Most of these false positives can be attributed to fluorescently excited edges of molecular clouds. The entire H_2 feature catalogue contains only 2 % of false positives, i.e. features that are not caused by emission from H_2 . These are mostly variable stars and image artefacts. Finally, the catalogue of jet/outflow features in Froeblich et al. (2015) is complete at the 95 % level for objects above the UWISH2 detection limit. Only a small number of low surface brightness features detectable in the UWISH2 data have not been included in the automatically generated catalogue.

We could identify driving source candidates for about 75 % of the MHOs and about 40 % of these objects are associated with groups or clusters of stars, while the remaining 60 % seem to be more isolated, indicating that clustered star formation could inhibit the formation of detectable larger outflows. We have identified 15 new star cluster candidates near the MHOs in the survey area. Of the WISE detected driving source candidates, about 20 % have positive slopes of their SED, i.e. are protostellar source candidates, while the remaining 80 % are most likely CTTs. This is also supported by their NIR colours. 70 % of the driving sources with multiple NIR K-band detections (UKIDSS GPS and 2MASS) show a variability of more than 0.1 mag and about 20 % of the sources vary by more than 0.5 mag over a timescale of several years.

The position angles of the identified outflows have a 99.99 %

probability to be drawn from a homogeneous distribution. For the typical bipolar outflow the two lobes have position angles within 5° . About 10% of the MHOs form X-shaped outflows which could be originating from binary sources (Lee et al. 2016).

The length ratio (short over long) of the lobes of the bipolar outflows have typical values between 0.6 and 1.0, with a median of 0.72. Only about 20% of objects are highly asymmetric with length ratios of less than 0.5. The flux ratios (short over long) typically show a much wider spread (between 0.2 and 5.0) and are not correlated with the length ratio.

We measured the length of all outflow lobes and investigated their distributions. We find that the length measurements typically used in the literature (end-to-end for bipolar outflows and source-to-end for single-sided flows) should be avoided. This is due to the typical asymmetry of the bipolar outflows. It causes the lobe length distributions and total length distributions to be different with a probability of 99.95%. There is no apparent difference in the lobe length distributions of outflows from younger and older driving source candidates.

The dynamical timescales of the outflows are up to 10 kyr, while the typical timescales associated with the gaps of large H_2 knots in the lobes correspond to 1–3 kyr. This indicates that neither FU-Ori or EX-Ori style outbursts are likely to be responsible for the formation of the larger H_2 knots seen in the typical outflows. Potentially the population of recently identified NIR eruptive variables, or MNors, with properties in-between FU-Ori and EX-Ori objects, could be the cause for the H_2 knot formation, if their as-yet unknown occurrence rate has the correct timescale.

The flux distributions of H_2 knots and outflow lobes is generally better fit by an exponential than by a power law. This is caused by a increased number of bright knots and lobes (above $30 \times 10^{-18} \text{ W m}^{-2}$) compared to the expectation for a power law distribution. There are no differences in the flux distributions for outflows from younger or older driving sources. The completeness limit for the detection of H_2 knots in the outflows is estimated as $10^{-18} \text{ W m}^{-2}$. The number of H_2 bright ($> 10^{-3} L_\odot$ in the 1–0S(1) line) outflows per square parsec in Aquila is comparable to investigations in the inner Galactic Plane.

In a future paper we will investigate these trends for a much larger sample of MHOs detected in the Cygnus X region where we expect a four- to five-fold increase in the number of MHOs. This will also be used to investigate if any of the trends are caused by environmental effects.

ACKNOWLEDGEMENTS

S.V.Makin acknowledges an SFTC scholarship (1482158). The United Kingdom Infra-Red Telescope is operated by the Joint Astronomy Centre on behalf of the Science and Technology Facilities Council of the U.K. The data reported here were obtained as part of the UKIRT Service Program.

REFERENCES

Bachiller R., 1996, *ARA&A*, 34, 111
 Bally J., Reipurth B., Davis C. J., 2007, *Protostars and Planets V*, pp 215–230
 Caratti o Garatti A., Giannini T., Nisini B., Lorenzetti D., 2006, *A&A*, 449, 1077

Casali M., Adamson A., Alves de Oliveira C., Almaini O., Burch K., et al 2007, *A&A*, 467, 777
 Contreras Peña C., Lucas P. W., Froebrich D., Kumar M. S. N., Goldstein J., Drew J. E., Adamson A., Davis C. J., Barentsen G., Wright N. J., 2014, *MNRAS*, 439, 1829
 Contreras Peña C., Lucas P. W., Kurtev R., Minniti D., Garatti A. C. o., Marocco F., Thompson M. A., Froebrich D., Kumar N., Stimson W., Navarro Molina C., Borissova J., Gledhill T., Terzi R., 2016, *ArXiv e-prints*
 Contreras Peña C., Lucas P. W., Minniti D., Kurtev R., Stimson W., Navarro Molina C., Borissova J., Kumar N., Thompson M. A., Gledhill T., Terzi R., Froebrich D., Garatti A. C. o., 2016, *ArXiv e-prints*
 Dame T. M., Hartmann D., Thaddeus P., 2001, *ApJ*, 547, 792
 Davis C. J., Froebrich D., Stanke T., Megeath S. T., Kumar M. S. N., Adamson A., Eisloffel J., Gredel R., Khanzadyan T., Lucas P., Smith M. D., Varricatt W. P., 2009, *A&A*, 496, 153
 Davis C. J., Gell R., Khanzadyan T., Smith M. D., Jenness T., 2010, *A&A*, 511, A24
 Frank A., Ray T. P., Cabrit S., Hartigan P., Arce H. G., Bacciotti F., Bally J., Benisty M., Eisloffel J., Güdel M., Lebedev S., Nisini B., Raga A., 2014, *Protostars and Planets VI*, pp 451–474
 Froebrich D., Davis C. J., Ioannidis G., Gledhill T. M., Takami M., Chrysostomou A., Drew J., Eisloffel J., et al. 2011, *MNRAS*, 413, 480
 Froebrich D., Makin S. V., Davis C. J., Gledhill T. M., Kim Y., Koo B.-C., Rowles J., Eisloffel J., Nicholas J., Lee J. J., Williamson J., Buckner A. S. M., 2015, *MNRAS*, 454, 2586
 Hatchell J., Fuller G. A., Richer J. S., 2007, *A&A*, 472, 187
 Ioannidis G., Froebrich D., 2012a, *MNRAS*, 421, 3257
 Ioannidis G., Froebrich D., 2012b, *MNRAS*, 425, 1380
 Khanzadyan T., Davis C. J., Aspin C., Froebrich D., Smith M. D., Magakian T. Y., Movsessian T., Moriarty-Schieven G. H., Nikogossian E. H., Pyo T.-S., Beck T. L., 2012, *A&A*, 542, A111
 Lawrence A., Warren S. J., Almaini O., Edge A. C., Hambly N. C., Jameson R. F., Lucas P., et al. 2007, *MNRAS*, 379, 1599
 Lee H.-T., Liao W.-T., Froebrich D., Karr J., Ioannidis G., Lee Y.-H., Su Y.-N., Liu S.-Y., Duan H.-Y., Takami M., 2013, *ApJS*, 208, 23
 Lee H.-T., Takami M., Duan H.-Y., Karr J., Su Y.-N., Liu S.-Y., Froebrich D., Yeh C. C., 2012, *ApJS*, 200, 2
 Lee J.-J., Koo B.-C., Lee Y.-H., Lee H.-G., Shinn J.-H., Kim H.-J., Kim Y., Pyo T.-S., Moon D.-S., Yoon S.-C., Chun M.-Y., Froebrich D., Davis C. J., Varricatt W. P., Kyeong J., Hwang N., Park B.-G., Lee M. G., Lee H. M., Ishiguro M., 2014, *MNRAS*, 443, 2650
 Lee K. I., Dunham M. M., Myers P. C., Arce H. G., Bourke T. L., Goodman A. A., Jørgensen J. K., Kristensen L. E., Offner S. S. R., Pineda J. E., Tobin J. J., Vorobyov E. I., 2016, *ApJ*, 820, L2
 Lucas P. W., Hoare M. G., Longmore A., Schröder A. C., Davis C. J., Adamson A., Bandyopadhyay R. M., et al. 2008, *MNRAS*, 391, 136
 Lyder D. A., Belton D. S., Gower A. C., 1998, *AJ*, 116, 840
 Majaess D., 2013, *Ap&SS*, 344, 175
 Richer J. S., Shepherd D. S., Cabrit S., Bachiller R., Churchwell E., 2000, *Protostars and Planets IV*, p. 867
 Scholz A., Froebrich D., Wood K., 2013, *MNRAS*, 430, 2910
 Snell R. L., Loren R. B., Plambeck R. L., 1980, *ApJ*, 239, L17
 Stanke T., McCaughrean M. J., Zinnecker H., 2002, *A&A*, 392, 239
 Vorobyov E. I., Basu S., 2006, *ApJ*, 650, 956

Walawender J., Bally J., Reipurth B., 2005, AJ, 129, 2308

APPENDIX A: MHO DATA TABLE

Table A1: Summary table of the MHO properties and their respective candidate driving sources. The table contains the following columns: i) the MHO number; ii) Right Ascension of the object (J2000) in degrees; iii) Declination of the object (J2000) in degrees; iv) Length of the outflow lobe(s) in degrees; v) Position angle of the outflow lobe(s) in degrees from North over East; vi) Integrated flux of the outflow lobe(s) or knots; vii) Type of outflow (B - bipolar, S - single-sided, K - single or group of knots without apparent source candidate); viii) Is the MHO associated with cluster or group of stars? ix) Source candidate identification; x) Likelihood P_S that source candidate is the real driving source in percent; xi) - xiii) Near-infrared JHK magnitudes of the source candidate; xiv) - xvii) Mid-infrared WISE magnitudes of the source candidate; xviii) - xxii) Is there a detection of the source candidate in the following surveys/catalogues: G - UKIDSS GPS, 2 - 2MASS, W - WISE, A - AKARI, I - IRAS? ⁽¹⁾ There are two values for all bipolar MHOs, one for each outflow lobe; ⁽²⁾ The unit of the fluxes is $10^{-19} \text{ W m}^{-2}$; ⁽³⁾ The first number refers to the magnitude in UKIDSS GPS, the second number to 2MASS. Note that same 2MASS detections might be blends of several sources. There are 4 objects with 2 GPS K-band epochs, we only list the first one in these cases as there is no variability above the 0.1 mag level between the two epochs in all cases.

MHO	Position (J2000) [deg]	Length ⁽¹⁾ [deg]	PA ⁽¹⁾ [deg]	Flux ^(1,2)	Type B/S/K	Cl. Y/N	Source ID	P_S [%]	J ⁽³⁾	H ⁽³⁾ [mag]	K ⁽³⁾	W1	W2 [mag]	W3	W4	G	2	W	A	I
MHO 1064	60.23841	53.356366	338.1	16	B	N	GPS439233255353	50	—	18.46	16.95	16.268	14.680	11.943	8.574	Y	N	Y	N	N
MHO 1065	60.39731	51.826319	166.3	57	B	N	GPS439239324153	90	19.48	—	15.55	13.899	11.382	8.249	4.871	Y	N	Y	Y	Y
MHO 1066	60.06662	51.504271	318.3	140	B	N	noname	90	—	17.21	—	14.600	13.658	12.568	9.142	N	N	Y	Y	N
MHO 1067	60.86852	51.863113	137.4	93	B	N	noname	90	—	—	—	10.485	8.559	5.725	2.995	Y	Y	Y	Y	Y
MHO 1068	60.83425	51.485619	188.7	51	B	N	GPS439239421916	90	18.59	15.37	12.81	10.485	8.559	5.725	2.995	Y	Y	Y	Y	Y
MHO 1069	60.76866	51.369731	70.1	195	B	Y	GPS439240314623	30	17.68	14.82	12.82	13.595	11.760	9.281	4.845	Y	N	Y	Y	N
MHO 1070	61.01052	51.378462	250.8	199	B	Y	unknown	—	—	18.51	16.36	—	—	—	—	N	N	N	N	N
MHO 1071	62.01052	52.378462	208.0	176	K	Y	unknown	—	—	—	—	—	—	—	—	N	N	N	N	N
MHO 1072	61.08369	51.391385	—	47	B	Y	GPS439241003473	20	17.92	15.28	13.35	11.209	9.418	6.419	2.522	Y	Y	Y	Y	N
MHO 1073	61.09325	51.396746	74.1	354	B	Y	GPS439241003473	20	16.86	15.26	13.34	11.209	9.418	6.419	2.522	Y	Y	Y	Y	N
MHO 1074	61.07890	51.376090	245.0	553	B	Y	GPS439241003473	20	17.92	15.28	13.35	11.209	9.418	6.419	2.522	Y	Y	Y	Y	N
MHO 1075	61.08764	51.374903	354.8	147	S	Y	GPS439241003473	20	16.86	15.26	13.34	11.209	9.418	6.419	2.522	Y	Y	Y	Y	N
MHO 1076	61.48638	51.485181	167.3	48	B	Y	J040420.08+512328.9	30	17.92	15.28	13.35	16.117	13.527	10.641	7.838	N	N	Y	Y	N
MHO 1077	61.48595	51.451418	324.5	229	K	Y	unknown	—	16.86	15.26	13.34	—	—	—	—	N	N	N	N	N
MHO 1078	60.98864	51.015907	194.7	114	K	Y	unknown	—	—	—	—	—	—	—	—	N	N	N	N	N
MHO 1079	61.48595	51.451418	—	140	B	Y	J040418.93+512233.9	90	—	—	—	14.306	13.644	8.544	6.434	N	N	Y	Y	N
	60.98864	51.015907	329.1	60	K	Y	unknown	—	—	—	—	—	—	—	—	N	N	N	N	N
	60.98864	51.015907	161.3	94	K	Y	unknown	—	—	—	—	—	—	—	—	N	N	N	N	N
	60.98864	51.015907	348.9	25	B	Y	GPS439240249378	10	13.19	11.59	10.05	8.401	7.029	4.332	1.845	Y	Y	Y	Y	N
	60.98864	51.015907	186.4	28	B	Y	GPS439241894456	20	12.26	11.08	9.84	12.678	9.685	6.912	3.818	Y	N	Y	N	N
			186.4	15	B	Y			—	18.67	16.16	—	—	—	—	—	—	—	—	—

Continued on next page

Table A1 – continued from previous page

MHO	Position (J2000) [deg]	Length ⁽¹⁾ [deg]	PA ⁽¹⁾ [deg]	Flux ^(1,2)	Type B/S/K	Cl. Y/N	Source ID	P _S [%]	J ⁽³⁾	H ⁽³⁾ [mag]	K ⁽³⁾	W1	W2 [mag]	W3	W4	G 2	W A I	
MHO 1080	61.83245	51.360570	89.8	140	S	N	J040719.78+512138.0	30	—	—	—	16.773	15.866	11.309	8.267	N	Y	N
MHO 1081	61.90227	51.265608	—	20	K	Y	unknown	—	—	—	—	—	—	—	—	N	N	N
MHO 1082	62.02223	51.281981	—	36	K	Y	unknown	—	—	—	—	—	—	—	—	N	N	N
MHO 1083	61.45279	50.778061	120.8	24	S	N	GPS439242797745	30	17.91	16.60	15.74	13.991	13.232	11.226	6.936	Y	N	N
MHO 1084	62.27979	51.080951	51.9	64	S	N	GPS439241917011	30	19.74	18.28	17.39	15.225	12.648	10.126	6.356	Y	N	N
MHO 1085	61.72960	50.496437	9.3	16	S	N	GPS439244391066	30	—	18.45	16.59	—	—	—	—	Y	N	N
MHO 1086	61.71765	50.513129	359.0	48	B	N	J040652.23+503047.2	90	—	—	—	15.569	13.013	8.887	3.659	N	Y	N
MHO 1087	61.63636	50.507554	175.1	125	B	Y	GPS439244244386	20	—	—	16.59	12.653	10.291	6.706	3.093	Y	N	Y
MHO 1088	61.87309	50.530046	138.8	19	B	N	J040729.54+503148.1	90	—	—	—	16.700	14.942	12.078	9.008	N	Y	N
MHO 1089	62.00873	50.538308	231.3	69	K	Y	unknown	—	—	—	—	—	—	—	—	N	N	N
MHO 1090	62.02896	50.523539	—	34	K	Y	unknown	—	—	—	—	—	—	—	—	N	N	N
MHO 1091	62.04327	50.522287	298.4	50	B	Y	GPS439244580755	60	16.53	14.21	12.29	10.749	9.534	6.540	3.538	Y	Y	Y
MHO 1092	61.36135	49.652435	125.0	18	B	Y	GPS439249569784	20	16.94	14.85	12.75	—	—	—	—	Y	N	N
MHO 1093	61.36233	49.650729	262.9	476	B	Y	GPS439249565961	20	—	18.52	16.86	—	—	—	—	Y	N	N
MHO 1094	61.36369	49.651530	7.3	41	B	Y	GPS439249565937	20	19.19	17.15	14.81	11.931	10.047	7.495	4.368	Y	N	N
MHO 1095	62.17080	49.795180	185.8	27	K	N	unknown	—	—	—	—	—	—	—	—	Y	Y	N
MHO 1096	63.33788	50.054994	26.5	24	K	Y	unknown	—	18.40	16.09	14.50	11.931	10.047	7.495	4.368	Y	Y	N
MHO 1097	65.56849	50.571718	212.2	72	B	N	GPS439243601173	30	18.17	15.71	14.30	—	—	—	—	Y	N	N
MHO 1098	65.57517	50.568972	333.7	107	K	N	unknown	—	—	—	—	—	—	—	—	Y	N	N
MHO 1099	65.46749	50.606260	157.6	27	B	N	GPS439243608737	50	—	—	—	—	—	—	—	Y	N	Y
			23.7	19	B	N			19.51	17.69	16.73	13.444	10.707	7.959	4.485	Y	N	Y
			203.9	48					—	—	—	—	—	—	—	—	—	—

Continued on next page

Table A1 – continued from previous page

MHO	Position (J2000) [deg]	Length ⁽¹⁾ [deg]	PA ⁽¹⁾ [deg]	Flux ^(1,2)	Type B/S/K	Cl. Y/N	Source ID	P _S [%]	J ⁽³⁾ [mag]	H ⁽³⁾ [mag]	K ⁽³⁾	W1	W2 [mag]	W3	W4	G 2	W A I Y/N	
MHO 2978	47.06005	56.776384	—	24	K	N	unknown	—	—	—	—	—	—	—	—	N	N	N
MHO 2979	47.02932	56.766349	9.1	64	B	N	GPS439222446979	90	19.16	16.95	14.77	12.942	10.997	8.782	5.788	Y	Y	N
MHO 2980	47.07636	56.393501	198.4	89	S	N	GPS439223566844	90	18.89	16.19	14.47	8.270	6.473	3.314	0.739	Y	Y	N
MHO 2981	51.94579	58.977700	335.4	49	B	N	GPS438826850299	40	16.75	13.88	11.05	16.106	16.956	10.599	8.744	Y	N	N
MHO 2982	51.86793	58.903200	—	46	S	Y	GPS438826615365	90	14.98	12.95	10.75	11.870	9.856	5.882	0.574	Y	Y	N
MHO 2983	50.73902	55.051985	308.2	187	S	N	GPS439226436484	60	16.67	15.27	14.34	15.266	13.278	11.248	5.136	Y	N	Y
MHO 2984	50.65753	55.060378	155.4	32	S	Y	GPS439226432804	30	—	—	—	10.261	8.720	6.349	2.724	Y	Y	N
MHO 2985	50.65956	55.061489	—	26	S	Y	GPS439226432818	20	17.79	15.22	13.43	11.261	9.720	7.349	3.724	Y	Y	N
MHO 2986	51.11426	55.203083	115.1	105	B	Y	GPS439225653298	10	16.30	14.73	13.16	—	—	—	—	Y	N	N
MHO 2987	51.11123	55.210352	295.8	118	B	Y	unknown	—	16.54	14.32	12.39	—	—	—	—	Y	N	N
MHO 2988	51.09660	55.210308	158.7	475	B	Y	unknown	—	—	17.39	14.85	—	—	—	—	Y	N	N
MHO 2989	50.98008	54.849785	338.1	78	K	Y	GPS439227089728	20	—	—	17.76	—	—	—	—	Y	N	Y
MHO 2990	51.45892	55.195615	—	22	K	Y	GPS439225484218	90	—	—	—	12.373	10.866	8.257	5.192	Y	Y	N
MHO 2991	51.23580	54.938369	286.8	71	B	N	GPS439227083972	90	17.96	15.43	13.69	10.856	9.243	5.171	2.878	Y	Y	N
MHO 2992	51.28495	54.956925	115.1	66	B	Y	unknown	—	15.90	15.42	13.71	—	—	—	—	Y	Y	N
MHO 2993	51.25459	54.979435	308.8	136	B	Y	unknown	—	19.09	16.53	14.22	—	—	—	—	Y	Y	N
MHO 2994	52.14302	55.180613	135.8	412	K	Y	unknown	—	18.67	16.02	14.01	—	—	—	—	Y	Y	N
MHO 2995	51.61656	54.682123	—	46	K	Y	unknown	—	—	—	—	—	—	—	—	Y	Y	N
MHO 2996	52.98990	55.645423	—	66	B	N	J032501.11+545845.8	90	—	—	—	14.289	11.809	7.805	3.861	N	N	N
MHO 2997	52.99320	55.645900	39.5	30	B	N	GPS439225550906	90	—	—	—	12.542	10.928	8.259	4.939	Y	Y	N
			219.1	18	B	Y	GPS439228061107	30	17.60	15.60	14.05	10.179	8.415	5.384	2.629	Y	Y	Y
			321.8	18	B	Y	GPS439224518813	20	16.91	15.18	13.79	11.282	10.510	7.244	5.039	Y	Y	N
			148.1	32	S	Y	0331584+553845	50	17.60	15.55	14.01	—	—	—	—	N	N	N
			321.3	187	S	Y			14.70	13.37	12.65	—	—	—	—	Y	Y	N
			132.5	384	B	Y			—	—	—	—	—	—	—	Y	Y	N
			90.9	—	B	Y			—	—	—	—	—	—	—	Y	Y	N
			326.1	14	B	Y			—	—	—	—	—	—	—	Y	Y	N
			150.9	19	B	Y			—	—	—	—	—	—	—	Y	Y	N

Continued on next page

Table A1 – continued from previous page

MHO	Position (J2000) [deg]	Length ⁽¹⁾ [deg]	PA ⁽¹⁾ [deg]	Flux ^(1,2)	Type B/S/K	Cl. Y/N	Source ID	P _S [%]	J ⁽³⁾	H ⁽³⁾ [mag]	K ⁽³⁾	W1	W2 [mag]	W3	W4	G 2	W A I	
MHO 2998	52.30408	54.716561	—	15	K	N	unknown	—	—	—	—	—	—	—	—	—	—	N
MHO 2999	52.88295	55.100457	69.9	41	S	N	J033131.90+550601.6	70	—	—	—	16.769	15.099	12.451	8.930	—	—	N
MHO 3600	64.81005	48.418351	101.3	9	B	N	GPS438834402010	90	—	17.85	15.81	14.185	11.977	9.048	5.982	—	—	Y
MHO 3601	64.80394	48.433302	279.1	12	K	N	unknown	—	—	—	—	—	—	—	—	—	—	N
MHO 3602	64.83847	48.420403	—	19	K	N	unknown	—	—	—	—	—	—	—	—	—	—	N
MHO 3700	53.29372	55.167976	53.7	19	B	Y	GPS439226302222	30	17.34	16.32	15.77	15.094	14.385	10.848	6.338	—	—	Y
MHO 3701	53.28411	55.171591	241.4	47	B	Y	GPS439225471182	40	14.00	12.90	11.96	10.326	8.940	5.771	3.031	—	—	Y
MHO 3702	53.28489	55.175693	239.4	28	B	Y	GPS439225471259	20	13.98	12.64	11.77	—	—	—	—	—	—	Y
MHO 3703	53.12653	54.845795	328.1	43	B	Y	GPS439227227879	70	18.05	17.10	16.53	—	—	—	—	—	—	Y
MHO 3704	53.03394	54.901486	150.0	158	B	N	—	70	14.35	13.31	12.06	10.371	9.136	6.441	4.273	—	—	Y
MHO 3705	52.89732	54.845318	124.8	128	B	N	—	70	14.63	13.40	12.22	16.278	14.704	12.372	9.117	—	—	Y
MHO 3706	55.36815	56.228536	312.0	74	B	N	J033208.14+545405.3	90	—	—	—	—	—	—	—	—	—	Y
MHO 3707	56.29465	54.526851	316.7	47	B	N	noname	10	—	—	—	—	—	—	—	—	—	N
MHO 3708	58.77886	53.798940	133.7	58	B	Y	noname	90	—	—	—	—	—	—	—	—	—	N
MHO 3709	58.87122	53.800635	89.6	18	B	N	noname	90	—	—	—	—	—	—	—	—	—	N
MHO 3710	58.88664	53.747850	264.5	10	B	N	J035506.92+534756.1	50	—	18.22	16.14	14.613	12.354	10.857	6.488	—	—	Y
MHO 3711	58.88604	53.741337	263.0	54	B	N	noname	90	—	—	—	15.665	13.532	10.359	5.410	—	—	Y
MHO 3712	58.88308	53.776865	68.3	28	B	N	noname	90	—	—	—	16.434	14.632	11.334	7.230	—	—	Y
MHO 3713	58.88825	53.767608	115.2	80	B	N	GPS439231466690	90	—	18.72	17.45	16.064	14.687	11.792	8.314	—	—	Y
MHO 3714	58.87778	53.763318	303.5	65	B	N	J035532.60+534428.9	90	—	—	—	—	—	—	—	—	—	Y
			274.7	8	K	N	unknown	—	—	—	—	—	—	—	—	—	—	—
			92.2	72	K	N	unknown	—	—	—	—	—	—	—	—	—	—	—
			269.2	55	K	N	unknown	—	—	—	—	—	—	—	—	—	—	—
			91.9	73	K	N	unknown	—	—	—	—	—	—	—	—	—	—	—
			271.1	46	K	N	unknown	—	—	—	—	—	—	—	—	—	—	—
			59.4	12	K	N	unknown	—	—	—	—	—	—	—	—	—	—	—
			235.3	16	K	N	unknown	—	—	—	—	—	—	—	—	—	—	—
			—	163	K	N	unknown	—	—	—	—	—	—	—	—	—	—	—
			—	221	K	N	unknown	—	—	—	—	—	—	—	—	—	—	—
			41.2	123	S	N	GPS439231463431	30	19.34	18.00	16.80	—	—	—	—	—	—	—

Continued on next page

Table A1 – continued from previous page

MHO	Position (J2000) [deg]	Length ⁽¹⁾ [deg]	PA ⁽¹⁾ [deg]	Flux ^(1,2)	Type B/S/K	Cl. Y/N	Source ID	P _S [%]	J ⁽³⁾	H ⁽³⁾ [mag]	K ⁽³⁾	W1	W2 [mag]	W3	W4	G 2	W A I	
MHO 3715	58.85462	0.00387	102.0	63	B	N	noname	30	—	—	—	—	—	—	—	N	N	N
MHO 3716	59.27117	0.00289	281.8	24	B	N	J035705.13+534654.0	30	—	—	—	17.474	15.323	11.830	9.092	N	N	N
MHO 3717	59.15515	0.00095	43.7	8	B	N	GPS439231567760	90	—	—	—	14.229	11.913	8.924	3.898	Y	N	Y
MHO 3718	59.05078	0.00083	229.4	11	B	N	GPS439231563437	30	—	19.26	16.57	13.951	12.134	8.746	5.188	Y	N	N
MHO 3719	59.01931	0.00042	12.1	12	B	N	GPS439231563011	30	18.35	16.89	15.44	14.574	14.057	11.438	7.815	Y	Y	N
MHO 3720	59.06760	0.00070	198.8	17	B	N	noname	50	—	—	—	—	—	—	—	N	N	N
MHO 3721	59.01390	0.00631	52.1	72	S	N	GPS439230543517	50	16.13	15.38	14.95	7.981	6.732	4.744	1.280	Y	Y	Y
MHO 3722	59.14762	0.00229	239.5	109	S	N	GPS439230543314	70	13.75	11.48	9.81	16.377	14.882	11.930	8.335	Y	N	N
MHO 3723	59.10104	0.00162	217.5	55	S	N	GPS439230545538	50	19.48	18.30	17.28	16.022	14.731	12.360	8.762	Y	N	N
MHO 3724	59.05799	0.00705	74.5	37	B	N	unknown	50	—	—	—	13.337	11.395	7.320	3.217	Y	N	N
MHO 3725	58.62680	0.00233	273.4	7	B	Y	unknown	50	—	—	16.84	—	—	—	—	N	N	N
MHO 3726	58.23936	0.00679	207.7	106	K	Y	unknown	—	—	—	—	—	—	—	—	N	N	N
MHO 3727	58.33467	0.00192	297.5	22	K	N	unknown	—	—	—	—	—	—	—	—	N	N	N
MHO 3728	58.80873	0.00791	176.4	25	S	N	GPS439234689441	50	—	18.52	16.69	14.396	11.795	9.003	5.446	Y	N	N
MHO 3729	58.33467	0.00818	176.4	25	S	N	noname	90	—	—	—	—	—	—	—	N	N	Y
MHO 3730	58.80873	0.03221	184.3	920	B	N	GPS439233238928	90	19.22	17.52	15.37	12.991	13.321	6.096	2.686	Y	Y	Y
MHO 3731	58.71942	0.00122	67.9	26	B	N	GPS439233906954	50	17.06	16.35	15.00	11.905	9.419	6.174	3.299	Y	N	Y
MHO 3732	58.71942	0.00094	253.4	42	B	N	GPS439233906954	50	—	18.55	15.11	11.905	9.419	6.174	3.299	Y	N	Y
MHO 3733	58.71942	0.00409	331.6	36	B	N	unknown	50	—	—	—	—	—	—	—	N	N	N
MHO 3734	58.71942	0.00568	141.0	40	B	N	unknown	50	—	18.55	15.11	11.905	9.419	6.174	3.299	Y	N	Y
MHO 3735	58.73051	0.05833	48.2	281	K	N	unknown	—	—	—	—	—	—	—	—	N	N	N
MHO 3736	58.73051	0.07911	229.0	557	K	N	unknown	—	—	—	—	—	—	—	—	N	N	N
MHO 3737	58.71409	0.00472	45.1	26	K	N	unknown	—	—	—	—	—	—	—	—	N	N	N
MHO 3738	57.90289	0.00758	220.1	93	B	Y	GPS439240289847	40	—	—	17.41	—	—	—	—	Y	N	N

Continued on next page

Table A1 – continued from previous page

MHO	Position (J2000) [deg]	Length ⁽¹⁾ [deg]	PA ⁽¹⁾ [deg]	Flux ^(1,2)	Type B/S/K	Cl. Y/N	Source ID	P _S [%]	J ⁽³⁾	H ⁽³⁾ [mag]	K ⁽³⁾	W1	W2 [mag]	W3	W4	G 2	W/A Y/N	I	
MHO 3735	57.90289 51.484970	0.00121 0.02414	74.6 267.1	16 74	B	Y	GPS439240289847	40	— —	— —	17.41 —	—	—	—	—	—	Y N	N N	N N
MHO 3736	59.96436 52.554540	0.00480 0.00340	156.4 340.9	141 124	B	N	GPS439235701408	50	17.24 16.59	15.84 15.20	14.58 13.36	12.980	10.904	7.912	4.006	Y Y	Y Y	Y Y	Y Y